So it is possible to virtually "dissect" an object, studying it from every angle. For this reason, the chemical composition of the studied materials is taken as a reference point. In this way, medical filters calibrated on human body have been chosen, with densities similar to the materials that coffins are made of (example: plaster is made, as the bones, by calcium; wood is "filled" by air, so lung). A striking example of this application, is the lung filter used on sarcophagus lid. This allowed to visualize and map all the original joints that connect the axes; it was also possible to, due to the different densities, to distinguish them from the restoration ones (see Figure 4).

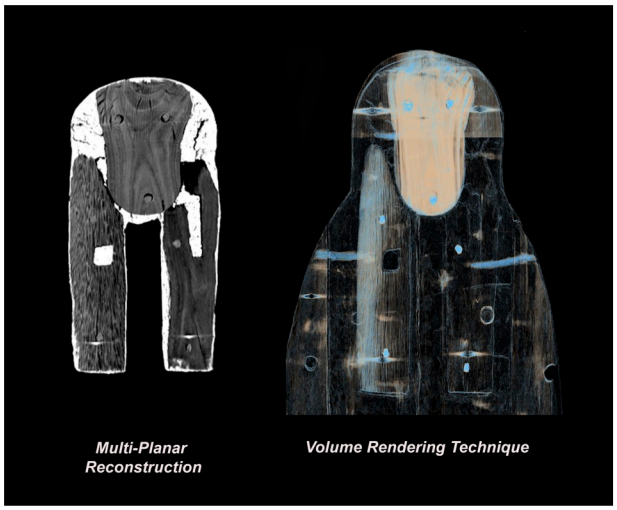

Figure 4: *Multiplanar Reconstruction (MPR) and Volume Rendering Technique (VRT) using lung filter.*

Thanks to this difference of densities, visible through the use of the pulmonary filter, it was possible to differentiate the types of wood that were used. It was perfectly observable because of the different colors. Other 3D filters used, namely the one for the cardiovascular system and the one for bones, have allowed to virtually "separate" the woody surface by the decorative one. This showed the cover anatomy; therefore, it was possible to enumerate the amount of axes that composed the coffin. Moreover, it was possible to virtually eliminate the large wooden support which had been anchored to the artifact during a XIX century restoration. This permitted to not submit the object to a dangerous restoration surgery for the removal of modern support. In this way, it was possible, to study depth preservation state and, therefore, to see the back of the artefact which, for the past two centuries, had been unknown. Undoubtedly, the variety of information obtained by this technique is very dependent on the object examined and, above all, on its size. In fact, the main limitation of this technique is precisely the diameter of the scanning tunnel (gantry), based on the size of human body, but on artefacts of small or medium size is possible to get astonishing results which are totally non-invasive. Surely, it was an enormous fortune to study such a rare and precious archaeological finding, but undoubtedly the use of MSCT has been a fundamental help to consider this artefact as an example of the Egyptian era reuse. In conclusion, an investigation in the field of Cultural Heritage using medical imaging equipment, allows to obtain useful structural information of the examined specimens, identifying false interpretations, even to the point of rewriting chapters of our history.

References

[1] Morigi M. P. et al.: *Application of X-Ray Computed Tomography to Cultural Heritage Diagnostics.* Applied Physics, **100**(3), 653–661 (2010).

[2] Longo, S. et al.: *Investigation of an Egyptian Mummy board by Using Clinical Multi-slice Computed Tomography.* Studies in Conservation, **63**(7), 383–390 (2018).

[3] Goldman L.W.: *Principles of CT: Multislice CT* Journal of Nuclear Medicine Technology, **36**(2), 57–68 (2008).

[4] McCollough, C. H. et al.: *Dual- and Multi-Energy CT: Principles, Technical Approaches and Clinical Applications.* Radiology, **276**(3), 637–653 (2015).

[5] Lindgren L. O.: *Medical CAT-scanning: X-Ray Absorption Coefficients, CT-Numbers and Their Relation to Wood Density.* Wood Science and Technology, **25**(5), 341–349 (1991).

Chiral optical tweezers for optically active particles in the T-matrix formalism

F. PATTI[1–2,*], R. SAIJA[1,2], M. A. IATÌ[2], O. M. MARAGÒ[2]

[1] *MIFT, Università di Messina, I-98156 Messina, Italy*
[2] *CNR-IPCF, Istituto per i Processi Chimico-Fisici, I-98158 Messina, Italy*

*Corresponding Author email: fpatti@unime.it

Abstract

Modeling optical tweezers in the T-matrix formalism has been of key importance for accurate and efficient calculations of optical forces and their comparison with experiments. Here we extend this formalism to the modeling of chiral optomechanics and optical tweezers where chiral light is used for optical manipulation and trapping of optically active particles. We show analytically that all the observables (cross sections, asymmetry parameters) are split into a helicity dependent and independent part and study a practical example of a complex resin particle with inner copper-coated stainless steel helices. Then, we apply this chiral T-matrix framework to optical tweezers where a tightly focused chiral field is used to trap an optically active spherical particle, calculate the chiral behaviour of optical trapping stiffnesses and their size scaling, and extend calculations to chiral nanowires and clusters of astrophysical interest.

Keywords: chirality, optical tweezers, T-matrix formalism.

Introduction

A chiral object is affected by the lack of symmetry under reflection [1]. Both radiation and material objects may have this property. The two chiral versions of an object are referred to as *enantiomers*. A great number of organic molecules, such as proteins and sugars, are characterized by optical activity, in fact gyrotropic studies possess a wealth of information, which has caused Barron to claim that "optical activity provides a peephole into the fabric of universe "[2]. Also the electromagnetic radiation can be considered a chiral field, expecially when we refer to left (LCP) and right (RCP) circular polarization. Its degree of chirality is measured through *optical chirality* C:

$$C = \frac{\epsilon_0}{2}\vec{E}\cdot\vec{\nabla}\times\vec{E} + \frac{1}{2\mu_0}\vec{B}\cdot\vec{\nabla}\times\vec{B}$$

Introduced by Lipkin in the eary sixties [3]. The main feature of the interaction between a chiral media and a chiral radiation is that depends on the chirality version involved. The goal of this work is to calculate the dynamics of the interaction between a chiral nanoparticles (e.g. a drop of water-sugar) and a chiral radiation (e.g. circular polarized).

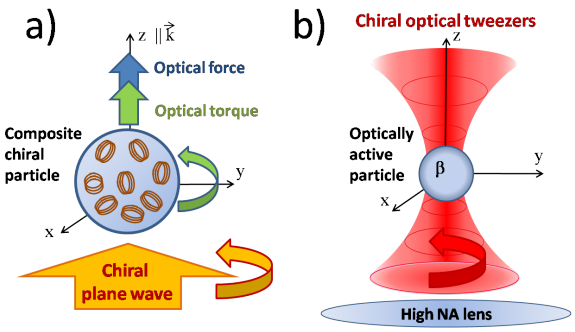

Figure 1: *We investigate chiral optical forces in two different configuration. In a) we investigate the optical force of chiral plane wave incident ona composite chiral sphere made of an epoxy resin with embedded copper-coated stainless steel helices. In b) a chiral Gaussian beam is tightly focused through a high numerical aperture lens and the optical behaviour of an optically active particle is investigated.*

Chiral optomechanics

For a macroscopic description of optical activity are sufficients the Drude-Born-Fedorov (DBF) consitutive relations [1]:

$$\vec{D} = \epsilon\vec{E} + \alpha\epsilon\vec{\nabla}\times\vec{E}$$
$$\vec{B} = \mu\vec{H} + \beta\mu\vec{\nabla}\times\vec{H}$$

If time symmetry is imposed, $\alpha = \beta$. The chirality parameter β is related with n_L and n_R (the refractive index for left and right circulary polarized waves):

$$\beta = \frac{\lambda}{4\pi}(\frac{1}{n_R} - \frac{1}{n_L})$$

So its real part is related with the different speed of propagation and its imaginary part with the different absorption of RCP and LCP EM waves. In addition, if the real pa mrt of β is positive the material is a right-handed medium and a LCP radiation propagates with a slower phase velocity, and viceversa. Expanding the fields in electric and magnetic multipoles, the natural optical activity can be considered as generated by appropriate superposition of these vector fields, involving interference between electric and magnetic multipoles. The components of these fields superposition constitute the so called 'optical activity tensors' that describe completely all phenomena related with chirality. On the basis of this approach, it is also possible to determine the optical forces generated in the chiral material-chiral radiation interaction, that depends on the extinction and scattering cross sections and of the anisotropy parameter:

$$\vec{F}_{Rad} = \frac{n}{c} I_{in}[\tilde{\sigma}_{ext} - \tilde{\sigma}_{scat}\tilde{g}_i]\vec{k}_i = \frac{n}{c} I_{in}\sigma_{RAD}\vec{k}_i$$

that can be separate in two parts, one helicity indipendet and the other helicity dependent:

$$\vec{F}^{\pm}_{Rad} = \vec{F}^{L}_{Rad} \pm \vec{F}^{h}_{Rad}$$

About the torque, we calculate the adimensional vector:

$$\vec{T} = \frac{16\pi^2}{n^2\lambda|E_0|^2\sigma_{ext}}\vec{\Gamma}_{RAD}$$

Where Γ_{RAD} is the torque at that position, E_0 is the amplitude of the incident field and σ_{ext} the extincion cross section.

Plane wave optomechanics

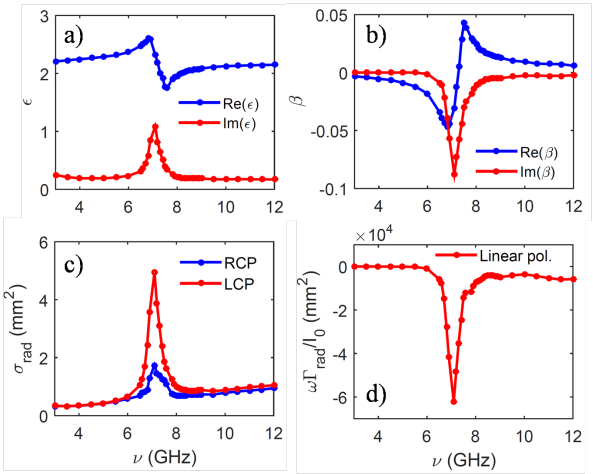

Figure 2: *A) Real and imaginary part of copper's electric permittivity . B) Real and imaginary part of chirality parameter. C) Radiation pressure cross section at different incident polarization. D) Torque cross section for linear incident polarization*

We apply this teoretical approach in the case of a plane wave incident on a chiral spherical nanoparticle. All the physical and chemical charateristics can be found in [5]. In figures 2 A-B we report the measure in the microwave range of the dielectric constant and of the chirality parameter β, performed at room temperature. In figure 2 C we report the σ_{RAD} in a spectral range around 6 GHz where the imaginary part of β has a deep minimum. Due to the spherical symmetry of the particle, the only component of F_{RAD} to be different from zero is in the direction of the incident field.
We can conclude that in a chiral material the intensity of the optical forces is directly linked to its dicroism. In figure 2 D, we report the results of Γ_{RAD} for linear polarization (along y axes). This leads to the conclusion that a DC spectrum directly reflects the performance of the spectrum of forces in that range of frequencies.

Chiral optical tweezers

As we are interested to the dynamical behaviour of chiral nanoparticles in an optical trap [4], we perform some simulation on the optical force for the case of an highly focalized field acting on a chiral sphere, located in the focal region. In particular, we use the angular spectrum rapresentation of a 10mW laser beam with a TEM_{OO} Gaussian profile at λ=632nm. The beam is focalized through an aplanatic lense, with numerical aperture NA=1.2 and filling factor f=2, in direction of the z axis. The radiation force acting on the nanoparticle is obtained applying the conservation of linear momentum. Since we are interested to the optical spectral range, we consider a typical case of a particle made with a material that exhibits optical activity in the visible, for this reason we chose a nanosphere with r=200 nm, refraction index 1.5 (immerse in water, n=1.33) and the chiral parameter 0.05, that correspond to the amino acids discovered in the Murchison meteorite. The dynamic quantities, σ_{RAD} and Γ_{RAD}, are calculated starting from their definition based on Maxwell stess tensor.

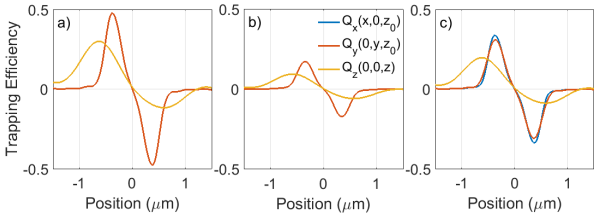

Figure 3: *Optical trapping efficiencies along the focal region axis, for LCP (A), RCP(B) and linear polarization (C)*

In figure 3, we report the computed components of σ_{RAD} in the focal region, for different state of polarization of the incident field. In this region, that extends between -1.4 and 1.4 micron along x, y and z axis, we note the harmonic behaviour of the components of radiation force, that in the vicinity of trapping point $r_0 = (0, 0, z_0)$, that

is the nominal focus position $z_0 = 0$, can be approximated through the expressions[6]:

$$\begin{cases} F_{rad,x}(x,0,z_0) = -k_x x \\ F_{rad,y}(0,y,z_0) = -k_y y \\ F_{rad,z}(0,0,z_0) = -k_z(z-z_0) \end{cases}$$

At this stage, it is very interesting to investigate the dependence of the 'trap stiffness k' on the dimension of the particle. The results of this study are reported in figure 4, where it is possible to compare the trap stiffnesses for different polarization states of the incident field. We notice that, unlike what happens in non-chiral case (see figura SI-x), the k-values are sistematically higher for the LCP polarization (the medium has a positive β), this indicates that the optical tweezers are an excellent experimental tool to discriminate the chiral nature of a nanoparticle. Moreover, at the same wavelenght, there is the possibility to optimize the trapping efficiency choosing an appropriate dimension of the investigated particle. For the case studied, we found the k-values at about ρ=300nm are up to 4 times higher than those obtained for $\rho > 500nm$.

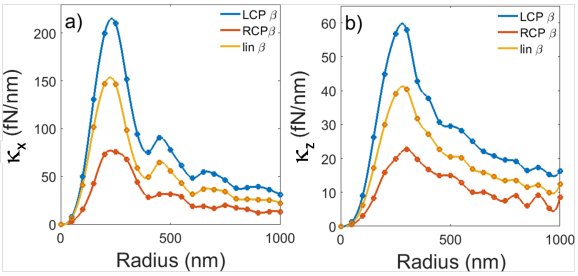

Figure 4: *Transverse (a) and axial (b) optical trapping stiffness as a function of the particle radius for 10 mW incident power*

Conclusions

In conclusion, we explored the connection between optical activity and optical forces in a general light scattering framework. We used the T-matrix formalism to enlighten the relation between chiral fields and observable cross sections. Thus, we applied this general formalism to study optical forces on an exemplar complex spherical resin particle with inner copper-coated stainless steel helices, and to the important case of optical tweezers on chiral particles of different shape and composition. In all cases, a chiral gap opens in the optical forces giving clear evidence of the connection between chiral optomechanics and optical activity. These examples are a starting point for more complex calculations on non-spherical, complex chiral particles in chiral and super-chiral optical that can be tightly confined as in optical tweezers or extended as the fields used in speckle optical tweezers.

Acknowledgement

This work was inspired by Ferdinando Borghese and it is dedicated to his memory. FP acknowledges support from a Research and Mobility Project of the University of Messina, RES-AND-MOB-2016-TORRIS1.

References

[1] Lakhtakia, A., Varadan, V., Varadan, V.: *Time-Harmonic Electromagnetic Fields in Chiral Media.* . Springer, 1989

[2] Barron, L. D.: *Molecular light scattering and optical activity.* Cambridge University Press, 2004

[3] Lipkin, D. M.: *Existence of a new conservation law in electromagnetic theory.* Journal of Mathematical Physics 5, 696-700, 1964

[4] Borghese, F., Denti, P., Saija, R.: *Scattering from Model Nonspherical Particles.* Springer, Berlin, 2007

[5] Ro, R., Varadan, V., Varadan, V.: *Electromagnetic activity and absorption in microwave chiral composites.* In IEE Proceedings H (Microwaves, Antennas and Propagation), vol. 139, 441-448 (IET, 1992).

[6] Jones, P. H., Maragò, O. M., Volpe, G.: *Optical tweezers: Principles and applications.* Cambridge University Press, Cambridge, 2015

The influence of the temperature on the dynamical Casimir effect

A. SETTINERI* AND S. SAVASTA

Department of physics, University of Messina, Italy

*Corresponding Author email: alessio.settineri@unime.it

Abstract

The interaction among the components of a hybrid quantum system is fundamental when considering the coupling of these components to an environment especially if the interaction strength is large. In this article, we apply a general master equation for arbitrary hybrid quantum systems interacting with thermal reservoirs to describe the influence of the temperature on the Dynamical Casimir Effect in ultrastrong coupling cavity optomechanics.

Keywords: Open quantum systems, USC regime (ultrastrong coupling regime), quantum optics, hybrid quantum systems, quantum rabi oscillations.

Introduction

According to quantum mechanics, a closed system always displays a reversible evolution. However, completely isolated systems does not exist. Thus, control and readout always requires some kind of coupling to the outside world, which leads to dissipation and decoherence (see, e.g., [3, 4]). As a consequence, realistic quantum systems should thus be regarded as open, taking into account the coupling to their environments. In this framework, a good description of the time evolution of an open quantum system can be provided by a quantum master equation [2, 5]. Usually, microscopic derivations of master equations start from the Hamiltonian dynamics of the total density matrix (for the system plus the environment). Then, tracing out the reservoir degrees of freedom, and introducing some approximations, allow to obtain a master equation describing the time evolution of the reduced density matrix for the system only [6]. A hybrid quantum system combines two or more physical components or subsystems [11], with the goal of exploiting the advantages and strengths of the different systems. An important requirement for the realization of a functional hybrid quantum system is the ability to transfer, with high fidelity, quantum states and properties between its different components. When deriving the master equation for a hybrid quantum system, the interaction between the subsystems is often neglected when considering their coupling to the environment. This results in the standard quantum-optical master equation [2, 5]. This procedure works well in the weak-coupling regime, and can be safely applied in the strong-coupling regime, when the density of states of the reservoirs and the system-bath interaction strengths are approximately frequency independent on the scale of the energy-level splittings induced by the interaction between the components. However, it has been shown that when the light-matter interaction increases up to the ultrastrong regime (USC) [7] this approach leads to unphysical predictions, e.g., excitations in the system even at zero temperature [1].

Model

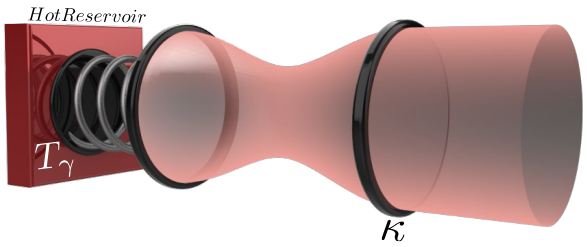

Figure 1: *Schematic of a generic optomechanical system where one of the mirrors of an optical cavity is thermally excited by means of an hot reservoir at temperature T_γ and can vibrate at frequency $\omega_{\rm m}$. In this conditions the system is able to emit photon pairs.*

We consider the case of a cavity with a movable end mirror (Figure 1) and focus on the simplest possible model system in cavity optomechanics, which has been used to successfully describe most of the experiments to date. Specifically, we consider a single mechanical mode of frequency $\omega_{\rm m}$ coupled to the lowest-frequency optical mode $\omega_{\rm c}$ of a cavity by radiation pressure.
Considering the creation (annihilation) mechanical and cavity bosonic operators respectively, $\hat{b}^\dagger$ ($\hat{b}$) and $\hat{a}^\dagger$ ($\hat{a}$), the system Hamiltonian ($\hbar = 1$) can be written as:

$$\hat{H}_{\rm S} = \hat{H}_0 + \hat{V}_{\rm om} + \hat{V}_{\rm DCE}\,, \qquad (1)$$

where,

$$\hat{H}_0 = \omega_c \hat{a}^\dagger \hat{a} + \omega_m \hat{b}^\dagger \hat{b} \tag{2}$$

is the unperturbed Hamiltonian,

$$\hat{V}_{om} = g\hat{a}^\dagger \hat{a}(\hat{b} + \hat{b}^\dagger) \tag{3}$$

is the standard optomechanical interaction Hamiltonian, and

$$\hat{V}_{DCE} = \frac{g}{2}(\hat{a}^2 + \hat{a}^{\dagger 2})(\hat{b} + \hat{b}^\dagger)\,, \tag{4}$$

is the perturbation term determining the DCE [9].
This last interaction term is often neglected when describing most of the optomechanics experiments to date.
This, is a very good approximation when the mechanical frequency is much smaller than the cavity frequency (which is the most common experimental situation), since $\hat{V}_{DCE}$ connects bare states with an energy difference $2\hbar\omega_c \pm \hbar\omega_m$ much larger then the coupling strength $\hbar g$.
Within this approximation, since the resulting Hamiltonian, $\hat{H}_0 + \hat{V}_{om}$, conserves the number of photons the system eigenstates can be written as:

$$|n, k_n\rangle = |n\rangle_c \otimes \hat{D}(n\beta)|k\rangle_m\,, \tag{5}$$

where $|n\rangle$ is the photon number and $|k_n\rangle$ represents the displaced Fock state determined by the displacement operator $\hat{D}(n\beta)$ with $\beta = g/\omega_m$.
However, when considering ultrahigh-frequency mechanical oscillators with resonance frequencies in the GHz spectral range, coupled to microwave resonators, the $\hat{V}_{DCE}$ term cannot be neglected, the number of photons is no longer conserved and the system eigenstates become no more analytical.
As shown in Ref. [9], such a system displays an energy level spectrum with a ladder of avoided level crossings arising thanks to the $\hat{V}_{DCE}$ contribution. For example, when $2\omega_c \simeq \omega_m$ [8]), the $\hat{V}_{DCE}$ gives rise to a resonant coupling between the states $|0, k\rangle$ and $|2, (k-1)_2\rangle$ with $k \geq 1$, converting a phonon into a photon pair.
Furthermore, when $\hat{V}_{DCE}$ is taken into account, the system Hamiltonian does not conserve the number of photons (notice that the phonon number is not conserved even in the standard optomechanical Hamiltonian). For example, the ground state of $\hat{H}_S$ contains photons, i.e., $\langle E_0|\hat{a}^\dagger \hat{a}|E_0\rangle \neq 0$. Therefore, in analogy to USC cavity QED, a careful treatment of dissipation and input-output theory is required since, if the standard photon and phonon operators were used to describe the interaction with the outside world, unphysical effects would arise.

The impact of temperature on the dynamical Casimir effect

The calculations in Ref. [9] were performed using a dressed master equation without the post-trace RWA, developed only for the case of zero-temperature reservoirs. Here, in order to study the influence of temperature on the energy conversion from phonons to photons, we instead apply a generalized master equation able to describe also the non zero-temperature conditions .
For our numerical calculation we consider a normalized optomechanical coupling $g/\omega_m = 0.1$, a mechanical damping rate $\gamma/\omega_m = 0.05$, and a cavity damping rate $\kappa = \gamma/2$. We focus on the avoided level crossing between the states $|0, 2\rangle$ and $|2, 0_2\rangle$ at $\omega_m \simeq \omega_c$. We consider the resonant condition, corresponding to the minimum level splitting: $\omega_c/\omega_m = 1.016$.
As in Ref. [9], we consider a continuous coherent drive of the mechanical oscillator,

$$\hat{H}_d = \Omega\left(\hat{b}e^{-\imath\omega_m t} + \hat{b}^\dagger e^{\imath\omega_m t}\right), \tag{6}$$

with frequency resonant with the oscillating mirror and amplitude $\Omega = \gamma/2$. The dynamics giving rise to the DCE is then described by the generalized master equation

$$\dot{\hat{\rho}} = -i\left[\hat{H}_S + \hat{H}_d, \hat{\rho}\right] + \mathcal{L}_{gme}\hat{\rho}\,, \tag{7}$$

where the Liouvillian superoperator $\mathcal{L}_{gme}\hat{\rho}$ contains all the collapse terms describing the system-reservoirs interactions and can be explicitly written as in Ref. [10].

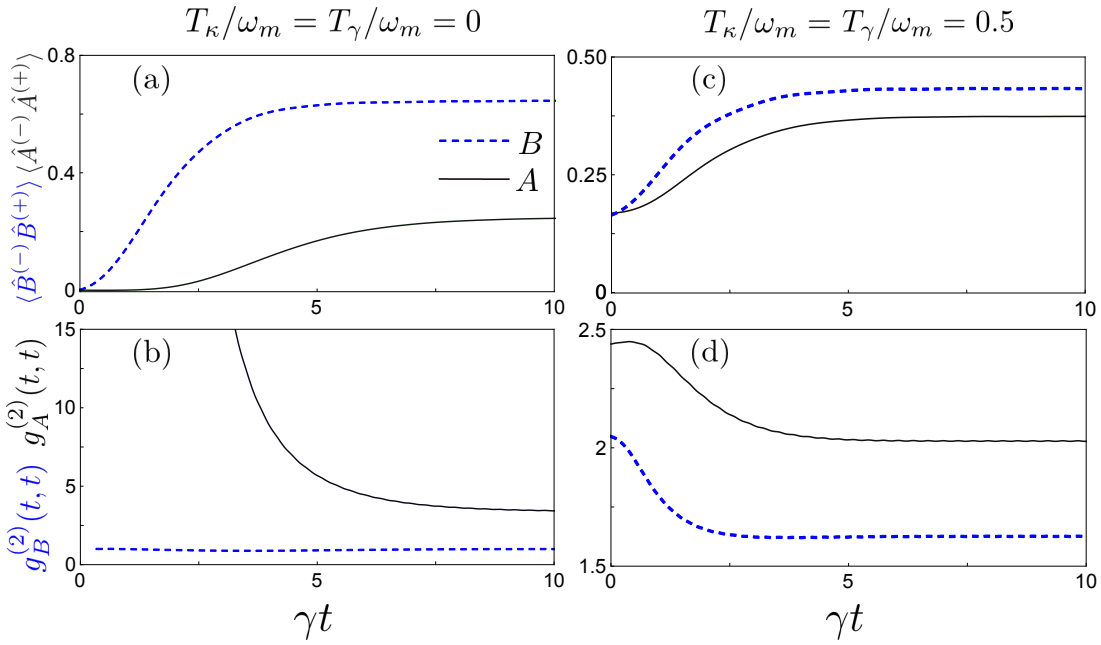

Figure 2: *Results for the dynamical Casimir effect at different temperatures. (a, b) System dynamics for* $\omega_c \simeq \omega_m$*, under coherent mechanical pumping, in perfect cooling conditions* $T_\gamma = T_\kappa = 0$*, starting the dynamics from the ground state. (c, d) The same, but with* $T_\gamma/\omega_m = T_\kappa/\omega_m = 0.5$ *and the initial state being the thermal state with* $T/\omega_m = 0.5$*. The blue dashed curves show the mean phonon number* $\langle \hat{B}^{(-)}\hat{B}^{(+)}\rangle$ *in (a, c) and the phonon-phonon correlation function* $g_B^{(2)}(t,t)$ *in (b, d). The black solid curves describe the mean cavity photon number* $\langle \hat{A}^{(-)}\hat{A}^{(+)}\rangle$ *in (a, c) and the zero-delay normalized photon-photon correlation function* $g_A^{(2)}(t,t)$ *in (b, d). All parameters for the simulations are given in the text.*

In Figure 2, we show the photonic and phononic populations, $\langle \hat{A}^{(-)}\hat{A}^{(+)}\rangle$ and $\langle \hat{B}^{(-)}\hat{B}^{(+)}\rangle$, and the relative two-photon and two-phonon correlation functions,

$$g_A^{(2)}(t,t) = \frac{\langle \hat{A}^{(-)}(t)\hat{A}^{(-)}(t)\hat{A}^{(+)}(t)\hat{A}^{(+)}(t)\rangle}{\langle \hat{A}^{(-)}(t)\hat{A}^{(+)}(t)\rangle^2}, \quad (8)$$

$$g_B^{(2)}(t,t) = \frac{\langle \hat{B}^{(-)}(t)\hat{B}^{(-)}(t)\hat{B}^{(+)}(t)\hat{B}^{(+)}(t)\rangle}{\langle \hat{B}^{(-)}(t)\hat{B}^{(+)}(t)\rangle^2}. \quad (9)$$

Figures 2(a, b) display the results of calculations done with zero-temperature reservoirs for both subsystems and starting the dynamics from the ground state. Figures 2(c, d) display the results of calculations for reservoirs with $T_\gamma/\omega_m = T_\kappa/\omega_m = 0.5$ and with the system initially in thermal equilibrium with those reservoirs.

At $T = 0$, with the system starting in its ground state, the photonic and phononic populations start from zero and, due to the coherent pumping, reach non-zero stationary values. The photonic correlation function $g_A^{(2)}(t,t)$ is initially much higher than two, suggesting photon-pair emission. Howver, as time goes on, it decreases significantly due to losses which affect the photon-photon correlations, and also due to the increase of the mean photon number (note that $g_A^{(2)}(t,t)$, owing to the squared denominator, is an intensity-dependent quantity). The mechanical correlation function $g_B^{(2)}(t,t)$, on the contrary, has an almost constant value ($g_B^{(2)}(t,t) \approx 1$), showing that the mechanical system is mainly in a coherent state produced by the pumping.

For reservoirs with non-zero temperature, the phonon and photon populations Figure 2(c), starting from their thermal-equilibrium values, equilibrate to lower steady-state values. This reduction of both populations originates from the increase of the decay rate of the coherent contributions with increasing temperature. We also note that the difference between the two steady-state values is reduced at higher temperatures, due to the thermal contributions. At $T \neq 0$, a fraction of the observed photons, as expected, does not come from the mechanical-to-optical energy conversion, but, trivially, from the photonic thermal reservoir.

This picture is confirmed by comparing the dynamics of the higher-order correlation functions [Figure 2(c, d)]. Specifically, at higher temperature, we observe a strong decrease of $g_A^{(2)}(t,t)$, showing that a reduced fraction of photons is emitted in pairs. However, the photon-photon correlation functions remains, even in the steady state, *higher* than the thermal value $g_A^{(2)}(t,t) = 2$. The phonon-phonon correlation starts from a value $\simeq 2$ corresponding to the initial incoherent thermal state and, as time goes on, decays to a stationary value higher than one due to the incoherent thermal excitations provided by the interaction with the thermal reservoirs.

Furthermore, in Figure 2(d), the photon-photon and the phonon-phonon correlation functions do not start from the same initial value. This effect is due to the $\hat{V}_{\rm DCE}$

term which, owing to its non-bilinear form, modifies the thermodynamic equilibrium of the initial state of the system. The $\hat{V}_{\mathrm{DCE}}$ contribution leads to a separation of the correlation-function values with size proportional to the temperature. This separation thus vanishes trivially for $T = 0$, when the $\hat{V}_{\mathrm{DCE}}$ term becomes negligible.
The results obtained clearly show that the generalized dressed master equation in Ref. [10] is able to describe dissipation in hybrid quantum systems with coexisting coherent phases (provided, e.g., by means of a continuous drive) and incoherent phases (provided, e.g., by thermal reservoirs or thermal-like pumping). The behaviour of the one- and two-photon correlation functions shows that signatures of the DCE can be observed even in the presence of a non-negligible amount of thermal noise. It thus demonstrates that this effect can be observed in a real experimental set-up, where perfect cooling conditions cannot be reached. Although the number of Casimir photon pairs produced depends on the thermal noise injected into the system, our results here show that the DCE remains detectable even at relatively high temperatures.

Conclusions

We applied a generalized master equation approach derived within the Born-Markov approximation, including the pure dephasing terms and without performing the usual post-trace RWA to study the influence of temperature on the conversion of mechanical energy into photon pairs (DCE) in an optomechanical system, recently described in Ref. [9] for zero-temperature reservoirs. In this case, we showed that the DCE can be observed also in the presence of a significant amount of thermal noise.

References

[1] F. Beaudoin, J. M. Gambetta, and A. Blais. Dissipation and ultrastrong coupling in circuit QED. *Phys. Rev. A*, 84:043832, 2011.

[2] H.-P. Breuer and F. Petruccione. *The Theory of Open Quantum Systems*. Oxford University Press, 2002.

[3] M. Brune, E. Hagley, J. Dreyer, X. Maître, A. Maali, C. Wunderlich, J. M. Raimond, and S. Haroche. Observing the progressive decoherence of the "meter" in a quantum measurement. *Phys. Rev. Lett.*, 77:4887–4890, Dec 1996.

[4] S. N. A. Duffus, V. M. Dwyer, and M. J. Everitt. Open quantum systems, effective Hamiltonians, and device characterization. *Phys. Rev. B*, 96:134520, oct 2017.

[5] C. W. Gardiner and P. Zoller. *Quantum Noise*. Springer, 3 edition, 2004.

[6] F. Haake. Statistical Treatment of Open Systems by Generalized Master Equations. In G. Höhler, editor, *Springer Tracts in Modern Physics*, pages 98–168. Springer, Berlin, Heidelberg, 1973.

[7] A. F. Kockum, A. Miranowicz, S. De Liberato, S. Savasta, and F. Nori. Ultrastrong coupling between light and matter. *to appear in Nat. Rev. Phys.*, 2018.

[8] A. Lambrecht, M.-T. Jaekel, and S. Reynaud. Motion Induced Radiation from a Vibrating Cavity. *Phys. Rev. Lett.*, 77:615, jul 1996.

[9] V. Macrì, A. Ridolfo, O. Di Stefano, A. F. Kockum, F. Nori, and S. Savasta. Nonperturbative Dynamical Casimir Effect in Optomechanical Systems: Vacuum Casimir-Rabi Splittings. *Phys. Rev. X*, 8:011031, 2018.

[10] A. Settineri, V. Macrì, A. Ridolfo, O. Di Stefano, A. F. Kockum, F. Nori, and S. Savasta. Dissipation and Thermal Noise in Hybrid Quantum Systems in the Ultrastrong Coupling Regime. jul 2018.

[11] M. Wallquist, K. Hammerer, P. Rabl, M. Lukin, and P. Zoller. Hybrid quantum devices and quantum engineering. *Phys. Scr.*, T137:014001, dec 2009.

Titanium oxynitride nanostructures prepared by laser ablation: synthesis and structural properties

D. SPUCCHES*, E. FAZIO, A. M. MEZZASALMA, F. NERI

Dipartimento di Scienze Fisiche, MIFT, Università di Messina, V.le F.S. D'Alcontres 31, 98166 S. Agata, Messina, Italy

*Corresponding Author email: dspucches@unime.it

Abstract

Pulsed laser ablation of nitride titanium (TiN) and dioxide titanium (TiO_2) targets were carried out in water using the 532 nm nanosecond laser radiation. In order to tune the compositional and structural properties of the nanomaterials, some other targets were home-prepared by simply mixing TiN and TiO_2 powders at different mass ratios (25/75 and 75/25). All these targets were irradiated with a laser fluence of 1.0 J/cm^2 and for an irradiation time of 15 min. The structural, morphological and compositional characteristics of the synthesized nanostructures were studied by means of the UV-vis optical absorption, visible Raman spectroscopies and the Electron Scanning Microscopy, operating in Transmission Mode (STEM). The properties of such nanostructures were investigated as a function of the synthesis history.

Keywords: Pulsed Laser Ablation, TiO_2,TiN, nanoparticles, Raman, SEM.

Introduction

TiO_2 is an effective and well-known photocatalyst for water and air purification, but its practical applications in visible light-assisted chemical reactions are hindered mainly by its poor visible light absorption capacity. However, the wide band gap of this material limits applications to UV light, which also confines the use of solar irradiation as the energy source. In the last years, literature data show the ability of nitrogen doping into TiO_2 to promote light absorption in the visible range, allowing the utilization of a large part of the solar spectrum [1]. All these synthesized $TiO_{2-x}N_x$ nanomaterials show highly reproducible photocatalytic activity, hence it has a potential for mass-production, and it is environmentally benign (no toxic ingredients). Nevertheless, it is still controversy if this doping is beneficial to the photocatalytic process, as well as the synthetic methods are not well stabilized yet to optimize the optical response. Thus, further development of this material is now underway, so it should be available to contribute to the human environment by reducing indoor VOCs (Volatile Organic Compounds) in the very near future.

Literature presents several methods to synthesize $TiO_{2-x}N_x$ colloids. One of the key challenges for this material is fabricating thin film devices using cost-effective and time-saving routes. Recently, to tackle this issue, a simple one-step, low temperature method has been developed for synthesizing mono-dispersed colloids of $TiO_{2-x}N_x$ nanocrystals which may be sprayed or printed on all kinds of substrates to create uniform thin films in large scale [2]. On the other hand, the 'in liquid' laser irradiation technique has been demonstrated to be an interesting method to easily increase the photocatalytic activity of TiO_2 [3] and other nanomaterials [4] towards the degradation of organic pollutants. We particularly evidence Ref. [5], reporting the activity of laser treated TiO_2 for the enhanced degradation of rhodamine B.

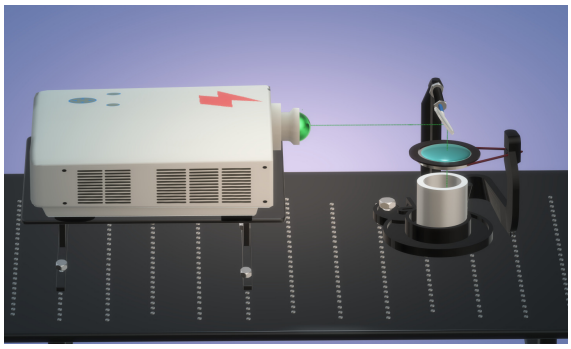

Figure 1: *Scheme of PLAL setup.*

In this work, we report about pulsed laser ablation (PLAL) processes in water, irradiating commercial targets of TiN and TiO_2 with the second harmonic of a Nd:YAG source, operating at the repetition rate of 10 Hz and at the pulse width of 6 ns. Aiming to obtain systems with variable physical-chemical properties, TiO_2 and TiN powders (purchased from Mateck) were mixed in different mass ratios. The powders were pressed and the obtained

targets were ablated in water. All the ablation products were also characterized by some techniques: conventional UV-vis optical absorption and visible Raman spectroscopies as well as Electron Scanning Microscopy (SEM), operating in transmission mode (STEM).

Experimental

TiN and TiO_2 powders were mixed at the different mass ratios of 75/25 and 25/75. Then, they have been pressed into a disk and the compacts were fired at around 250^0C for 1 hour. Pulsed laser ablation (PLAL) processes of the $TiO_{2-x}N_x$ pressed powders as well as of the pristine TiN and TiO_2 targets were carried out in deionized water (H_2O). The second harmonic (532 nm) of a laser operating at the repetition rate of 10 Hz and at the pulse width of 6 ns was used. The target was irradiated with a laser fluence of 1.0 J/cm^2 and for an irradiation time of 15 min. A scheme of PLAL setup is shown in Figure 1.

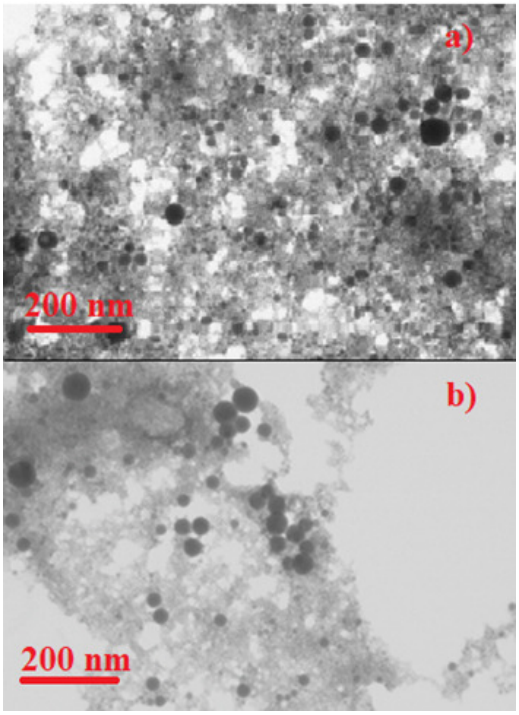

Figure 2: *STEM images of the colloids prepared ablating: a) mixed TiN/TiO_2 powders at the 25/75 mass ratio; b) commercial TiN target in water.*

The optical absorption of the colloids was analyzed by means of a Perkin–Elmer Lambda 750 UV– vis spectrometer in the 190-900 nm range using quartz cells. STEM images were taken by a scanning electron microscope (ZEISS; model Merlin Gemini 2) operating at an accelerating voltage of 30 kV and a working distance of 4 mm. A fraction of the synthesized colloids was deposited on silicon substrates and nickel grids to carry out Raman and STEM characterizations. To carry out Raman measurements, the 532 nm diode laser line was used as excitation source and the spectra were collected by a Charge Coupled Device (CCD) device, for an integration time of 80 sec.

Results and Discussion

The average particle size, shape and size distribution of the as-prepared $TiO_{2-x}N_x$ nanoparticles were investigated using the STEM technique. STEM image of the colloids prepared ablating the mixed TiN/TiO_2 powders at the 25/75 mass ratio is shown in Figure 2(a). An high density of dispersed nanoparticles, with a spherical shape and size of around 10-30 nm, characterizes these colloids. A similar morphology is shown by the sample prepared ablating the target made from the 75/25 mass ratio TiN/TiO_2 powders (not shown). In this case, some of the nanoparticles aggregate together. Finally the colloids, synthesized by an high purity (99.99%) commercial TiN target in water, shows some dispersed spherical nanoparticles of about 40 nm in size (see Figure 2(b)).
In Figure 3 are shown UV-vis optical absorbance and micro-Raman spectra. The colloid, obtained in water by the TiN rod target, is transparent (over 90 %) in the visible range with a sharp absorption edge at about 350 nm. Otherwise, a broad band at around 420 nm characterizes the sample prepared from the TiO_2 powder target. A similar blu-shifted and narrow band is evident in the colloids prepared using the pressed and sintered target with a (25/75) TiN/TiO_2 mass ratio. The optical absorption contribution in the UV region is the TiO_2 characteristic edge [3] while the increase of the absorbance values in the visible-light range is justified taking into account the nitrogen addition into the titanium oxide matrix [1, 6]. Moreover, we observe that the 420 nm band is totally absent in the colloids prepared using the TiN powder or a target with a (75/25) TiN/TiO_2 mass ratio. Despite this, an increase of the optical absorbance signal at the higher wavelength ($>$ 700 nm) is observed for these last two colloids. Although preliminary, these experimental evidences indicate that we are on the right track to achieve the objective of increasing the optical response in the visible region.
Raman spectroscopy is a powerful technique for characterizing the micro-nanostructures of the TiO_2 based materials [7]. In Figure 3(b) is shown the Raman spectra of the colloids prepared ablating in water the (25/75) and the (75/25) TiN/TiO_2 mass ratio targets. The sample obtained using the pristine TiN target (not shown) presents the same contribution of the (75/25) mixed target. In the inset of the figure, we report the typical Raman features of the rutile and anatase TiO_2 phases. According to literature data [8], the anatase phase of TiO_2 has six Raman bands at 144 cm^{-1} (E_g), 197 cm^{-1} (E_g), 399 cm^{-1} (B_{1g}), 513 cm^{-1} (A_{1g}), 519 cm^{-1}(B_{1g}) and 639 cm^{-1} (E_g), and the rutile phase has four Raman bands at 143 cm^{-1} (B_{1g}), 447 cm^{-1} (E_g), 612 cm^{-1} (A_{1g}), and 826 cm^{-1} (B_{2g}). Here, both samples show Raman spectra characterized by a mix of the pure anatase and rutile phase. However, the bands so enlarged suggested that the low frequency peaks below 400 cm^{-1} and the high

frequency mode around 550 cm^{-1} can be partially due to the Ti-N acoustical and optical phonons, respectively [9]. In particular, the colloid obtained by the (25/75) TiN and TiO_2 powders target shows a significant blue-shift and a broadening of the observed peaks. This evidence indicates a structural rearrangement with a probably small amount $TiO_{2-x}N_x$ formation on the TiO_2 surface. Thus, to investigate about the surface chemical bonding configurations, we are currently carrying out X-ray photoelctron spectroscopy (XPS) measurements, the results of which will be the subject of a subsequent work.

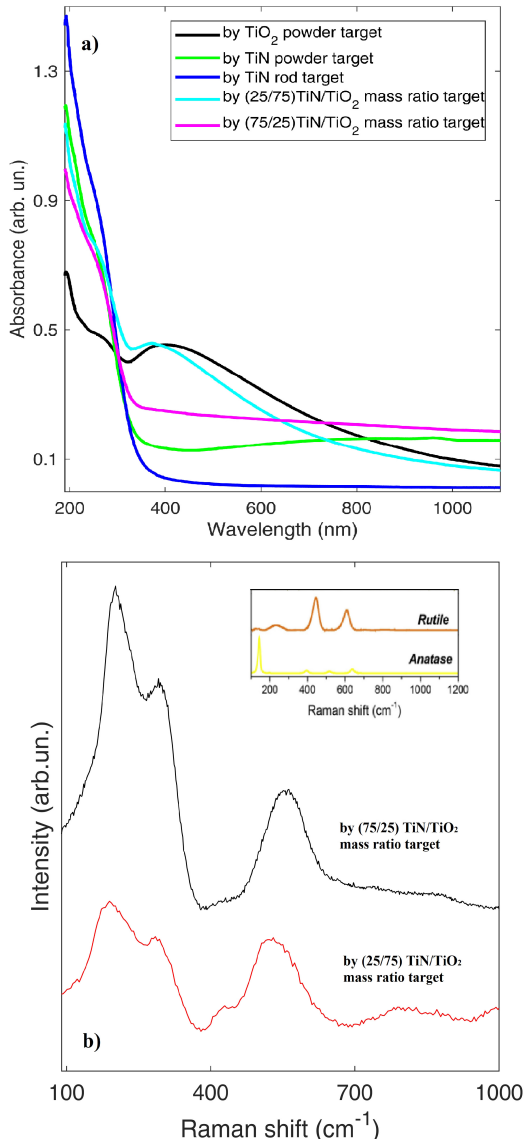

Figure 3: *a) UV-vis optical absorbance and b) Raman spectra of the PLAL synthesized colloids.*

Conclusion

$TiO_2 - xN_x$ nanocolloids, chemically and morphologically stable, were prepared in water carrying out nanosecond pulsed laser ablation processes. The results of STEM analyses revealed that the synthesized samples were composed of nearly spheroidal nanoparticles with a size below 40 nm. Raman features arising from anatase and rutile titania vibration modes were mainly detected for the sample obtained mixing the TiN/TiO_2 powders. A blue-shift of the TiO_2 features as well as the presence of some vibrational modes typical of TiN materials were observed when we have ablated the pristine TiN target in water. Although preliminary, these results are interesting for the possibility of tuning the compositional, structural and optical properties of the $TiO_2 - xN_x$ colloids. Hence, we conclude that by an accurate control of the optical properties, a $TiO_2 - xO_x$ based absorbing coating could be fabricated to ultimately achieve an high performance solar selective $TiO_2 - xO_x/SiO_2$ antireflection layers.

References

[1] Ansari, S. A., Khan, M. M., Ansaric, M. O., Cho, M. H.: *Nitrogen-doped titanium dioxide (N-doped TiO_2) for visible light photocatalysis.* New J. Chem., **40**, 3000–3009 (2016).

[2] Jiang, Z. Shi, H., Yang, G., Xiao, T., Jones, M. O., Edwards, P. P.: $3^r d$ International Nanoelectronics Conference (INEC), (2010)

[3] Filice, S., Compagnini, G., Fiorenza, R., Sciré, S., D'urso, L., Fragalà, M. E., Russo, P., Fazio, E., Scalese, S.: Journal of Colloid and Interface Science, **489**, 131–137 (2017).

[4] Buccheri, M. A., D'Angelo, D., Scalese, S, Spanò, S. F., Filice, S., Fazio, E., Compagnini, G., Zimbone, M., Brundo, M.V., Pecoraro, R. Alba, A., Sinatra, F., Rappazzo, G., Priviteera, V. : Nanotechnology, **27**, 245704–245716 (2016).

[5] Chen, X., Zhao, D., Liu, K., Wang, C., Liu, L., Li, B. Zhang, Z., Shen , D.: ACS Appl. Mater. Interfaces **7**, 16070–16077 (2015).

[6] Cao, Y. Q., Zhao, X. R., Chen, J., Zhang, W., Li, M, Zhu, L., Zhang, X. J., Li, A.:Scientific Reports, **8**, 12131 (2018).

[7] Frontera, P., Malara, A., Stelitano, S., Leonardi, S. G., Bonavita, A., Fazio, E., Antonucci, P., Neri, G., Neri, F., Santangelo, S.:Mat. Chem. And Phys. **170**, 129-137 (2016).

[8] Franck, m., Celis, J-P., Roos, J. R.: J. Mater. Res. **10** (1), 119 (1996).

[9] Spengler, W., Kaiser, R., Christensen,A.N., Muler-Vogt, G.:Phys. Rev. **B 17**, 1095 (1978).

Seminari del Dottorato di Ricerca in Fisica

(Svolti nel 2018)